Materials Today Communications 41 (2024) 110337

Contents lists available at ScienceDirect

Materials Today Communications

journal homepage: www.elsevier.com/locate/mtcomm

Insight into layer formation during friction surfacing: Relationship between deposition behavior and microstructure

Marius Hoffmann [a], Zina Kallien [a,b,*], Eduardo Antunes Duda [a,c], Benjamin Klusemann [a,b]

[a] Helmholtz-Zentrum Hereon, Institute of Material and Process Design, Solid State Materials Processing, Max-Planck-Straße 1, 21502 Geesthacht, Germany
[b] Leuphana University Lüneburg, Institute for Production Technology and Systems, Universitätsallee 1, 21335 Lüneburg, Germany
[c] Laboratório de Metalurgia Física, LAMEF, Universidade Federal do Rio Grande do Sul, UFRGS, Porto Alegre, RS, Brazil

ARTICLE INFO

Dataset link: https://doi.org/10.5281/zenodo.13734042

Keywords:
Friction surfacing
Layer formation
Microstructure
Texture
Aluminum

ABSTRACT

Friction surfacing (FS) is a solid state layer deposition technique with a simple setup, presenting advantages compared to fusion-based approaches. Previous investigations showed microstructural gradients along layer width and thickness. The current study provides new insight into the FS layer formation for aluminum and its relation with the microstructure evolution. Special consumable studs containing two different aluminum alloys were used to visualize the different materials in the resulting deposit. The investigation was performed at different process parameters, revealing some fundamental material flow characteristics. The layer center presents inner stud material, where advancing side and top are formed by outer stud material. The bottom and retreating side present a mixture of inner and outer stud material. The part of the layer that is formed by the outer material, presumably undergoes higher strain rates during deposition, presenting finer grains. The top of FS layers shows a pronounced texture, *i.e.* shear texture components, compared to the other parts with random texture. This phenomenon can be related to the shearing of the stud material between already deposited material below and the stud at its rear edge. Overall, the FS layer formation characteristics revealed in this study are directly related to local microstructural properties.

1. Introduction

Solid state layer deposition approaches offer several advantages compared to fusion-based processes. The remaining challenges of fusion-based approaches are complex, for instance for aluminum alloys, porosity formation or heterogeneous microstructures consisting of strongly oriented columnar grains can be present [1]. Porosity is often formed in the inter-layer regions, *i.e.* between subsequent layers, resulting in anisotropic behavior of the deposited structure [2]. Additionally, strong thermal gradients within the structure, resulting from the high process temperatures necessary for material melting, might lead to hot cracking [3] as well as significant residual stresses and distortion [4]. Since layer deposition techniques are the basis for additive manufacturing approaches, the effects during subsequent layer deposition can detrimentally influence the properties of the final structure.

Most of the above mentioned issues can be avoided via solid state deposition techniques, in particular due to the lower process temperatures [5]. The friction stir-based solid state layer deposition techniques are suitable to process a wide range of similar and dissimilar material combinations, even materials considered non-weldable [6]. One of these techniques is the friction surfacing (FS) process, where its feasibility for multi-layer or solid state additive manufacturing structures has already been shown [7,8]. The solid state layer deposition via FS is based on friction and plastic deformation and does not necessitate a non-consumable tool. Instead, a consumable stud is used to deposit a layer. The FS process can be divided in two phases: In the first phase, the plasticizing phase, the consumable stud is positioned above the substrate surface and experiences a rotational speed and an axial force. The rotating stud is pressed on a substrate, which leads to frictional heat at the materials' interface and deformation and plasticizing of the consumable stud's tip. When the tip of the stud is plasticized, the second process phase is initiated, the deposition phase. Here, a relative translational movement between plasticized consumable material and substrate is superimposed and enables the deposition of the consumable stud material onto the substrate as a layer. The process is ended with the retraction of the remaining stud material when the desired deposition length is achieved.

* Corresponding author at: Helmholtz-Zentrum Hereon, Institute of Material and Process Design, Solid State Materials Processing, Max-Planck-Straße 1, 21502 Geesthacht, Germany.
E-mail address: zina.kallien@hereon.de (Z. Kallien).

https://doi.org/10.1016/j.mtcomm.2024.110337
Received 24 April 2024; Received in revised form 12 August 2024; Accepted 4 September 2024
Available online 7 September 2024

The characterization of multi-layer structures built via the FS principle is available in the literature and presents promising mechanical properties as, for instance, Rath et al. [9] could not observe a significant directional dependency in terms of tensile strength. The FS deposited layers typically present a significantly refined microstructure enabled by dynamic recrystallization [10], leading to improved mechanical properties. The microstructure of a FS deposited layer shows slight trends along layer width and thickness and also depends on the process parameters as reported by Rahmati et al. [11]. The study [11] presents a difference in grain size between upper and lower part of the layer, where a decrease in average grain size for decreasing axial feeding rate, increasing travel speed and decreasing rotational speed for FS of AA2024 over AA1050 was reported. In terms of rotational speed affecting the average grain size, similar observations were reported by Yu et al. [12] for FS of AA6061 over carbon steel. A recent investigation by the authors [13] in terms of average grain size along build direction for multi-layer FS structures revealed that the grains are slightly smaller on top and bottom of the individual layers, being a fundamental characteristic of FS layers as this could be shown for two different aluminum alloys, *i.e.* AA2024 and AA5083, and for different process parameters. Ehrich et al. [14] investigated the grain size within the FS layer along width, *i.e.* on the advancing side, center and retreating side. The analysis showed smaller grains at the advancing side of the deposit compared to retreating side and center. Overall the slight gradients in grain size were associated with the complex material flow during FS layer deposition [15], which leads to varying plastic strain and temperature condition not only for varying process parameters but also along width and thickness within a layer.

The layer formation during the deposition process still needs an in-depth investigation to understand the aforementioned trends in FS deposit's microstructure. This knowledge is crucial to tailor the microstructure and therefore the properties of a deposited structure, which is still an open subject in literature. The novelty in the present study lies in the use of special consumable studs consisting of two different aluminum alloys to analyze the material flow behavior in depth. Powder [15,16] or chip material [17], which is inserted in the consumable stud, can also be used as tracer; however this can cause instabilities in the material flow [15]. Similar approaches were also used for other friction-based solid state layer deposition techniques, for instance, additive friction stir deposition [18]. Even though the principle of this layer deposition technique is closely related to FS, there are significant differences in the deposition mechanism due to the use of a non-consumable tool, which is assumed to drastically affect the material flow. For that reason, the discussion of the results obtained by this work will not include an in-depth comparison to results for other solid state layer deposition technologies available in the literature.

Compared to the powder and chip materials recently used in the literature [15–17], which cause process instabilities, the special stud configuration used in this study enables a continuous deposition process. A similar approach was applied by Fukakusa [19] using stainless steels with different ratios of the two materials to investigate which parts of the stud form layer and flash. Even though the use of two different materials in one stud configuration can affect the process behavior due to different thermal softening (rates) and flow stresses of the two materials used, it allows to continuously visualize and analyze the layer formation for different process parameters in this study. In addition, samples obtained from stop action experiments are analyzed at different positions and provide a valuable insight into the material transfer from consumable stud into the layer. The fundamental characteristics of the FS layer formation are identified and interlinked with microstructural characteristics as well as hardness. For reference purposes, results were also obtained for deposits from single material studs. An in-depth understanding of the FS deposition process is gained and correlated with previous findings, which is important knowledge when developing the FS process further towards application.

Table 1
Overview of stud configuration and process parameters.

Sample	Stud material	Force [kN]	Rotational speed [rpm]	Travel speed [mm/s]
1	AA2024/AA5083	8	800	6
2	AA2024/AA5083	6	800	6
3	AA2024/AA5083	10	800	6
4	AA2024/AA5083	8	600	6
5	AA2024/AA5083	8	1000	6
6	AA2024/AA5083	8	800	4
7	AA2024/AA5083	8	800	8
8	AA5083	8	800	6
9	AA2024	8	800	6
10	AA5083	8	600	6
11	AA2024	8	600	6
12	AA5083	8	1000	6
13	AA2024	8	1000	6

2. Materials and methods

The FS layers in this study were deposited force-controlled at room temperature using the friction welding machine RAS (Henry Loitz Robotik, Germany). AA2024-T3 substrates (length 250 mm, width 100 mm, thickness 3.7 mm) were used for all experiments of this study. An 8 mm thick AA2024 plate was placed below the substrate as a backing. In order to visualize the layer formation behavior, a special stud configuration was used, which consists of two parts, *i.e.* an inner and an outer material. For the outer part of the stud (length 100 mm, diameter 20 mm), AA2024-T351 was used, presenting an 8 mm hole for the inner part. The inner part of the stud (length 100 mm, diameter 8 mm) was AA5083-H112, which was inserted in the outer part, Fig. 1(b). This stud configuration was used to visualize the flow of the different materials during the layer formation and to investigate the influence of the three main process parameters, *i.e.* rotational speed, axial force, and travel speed, Table 1. In addition and for comparison purpose, common studs, *i.e.* consisting only of one single material, (length 100 mm, diameter 20 mm) were used for AA2024-T351 as well as AA5083-H112 at previously used process parameters, see Fig. 1(a) and Table 1. The common studs are used to validate the results obtained from the layer formation investigation, as these results represent the general layer formation behavior during conventional FS. The deposition length for all layers was selected to be 90 mm. The deposition processes were stopped without retraction of the stud from the layer after achieving the pre-programmed deposition length. This stop action procedure[1] allows the investigation of cross and longitudinal sections where the consumable stud material is still attached to the corresponding deposit. Especially for the stud configuration with different inner and outer material, this method allows valuable insights into the layer formation behavior *i.e.* the material flow during FS layer deposition. The obtained samples were investigated at different positions, which allow a quasi-3D analysis of the layer formation for the respective cross and longitudinal sections.

After layer deposition, cross sections were cut from the deposits and were prepared using common metallographic practices, *i.e.* grinding with 320 and 4000 grid SiC paper for two minutes each, followed by polishing with 1 μm diamond suspension for four minutes. The samples for the electron backscatter diffraction (EBSD) investigation underwent vibration polishing using Vibro-Met2 vibratory polisher (Buehler, Germany) with a 0.02 μm silica suspension for additional four hours.

The different materials within the layers are revealed by etching, using a solution containing 5.0% sulfuric acid (H_2SO_4), 2.5% hydrofluoric acid (HF) and 92.5% distilled water (H_2O) for 10 seconds. The

[1] No additional cooling was applied during stop action of the deposition process.

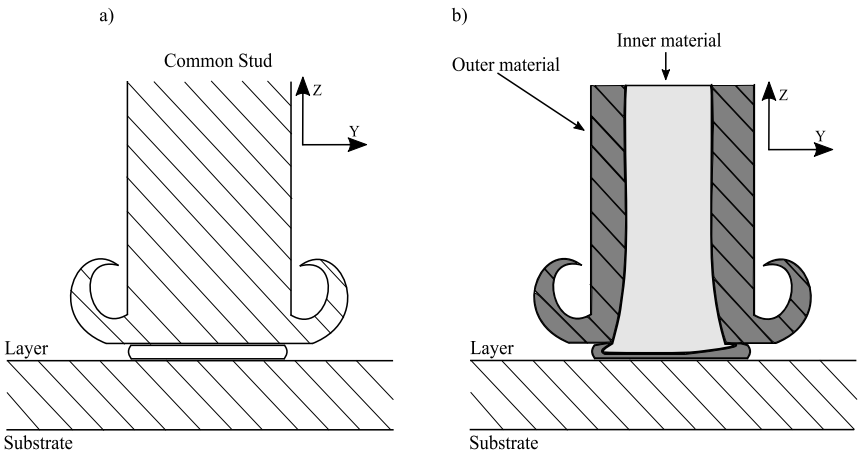

Fig. 1. Schematic of stud material used, with common stud material cross section (a) and stud with outer and inner material cross section (b).

solution etches AA2024 faster than AA5083, leading to an enhanced contrast using the optical microscope VHX-6000 (Keyence, Germany). The images of the cross sections were further analyzed using Trainable Weka Segmentation plugin for ImageJ, which enables the segmentation by the stud materials, coloring each material differently. Based on the number of pixels, the segmentation allows the calculation of the total area and percentage of AA2024 and AA5083 present in the deposit.

The scanning electron microscope Quanta 650 FEG (Thermo Fisher Scientific, USA) equipped with an EDAX EBSD detector of the Velocity series and an EDAX Octan Elect Super energy-dispersive X-ray spectroscopy (EDS) detector (both AMETEK, USA) was used for the microstructure investigation and the chemical analysis of the layers, respectively. The analysis of the EBSD data was performed using the MTEX toolbox, version 5.8.1, in MATLAB (The Mathworks, USA). Grains are defined by a misorientation angle of 5° and a minimum number of 5 pixels. Grains with a misorientation angle less than 15° are considered as low angle grain boundaries (LAGBs), whereas grains with a higher misorientation angle represent high angle grain boundaries (HAGBs).

Hardness testing was conducted using an automated hardness machine DuraScan 70 G5 (EMCO-TEST GmbH, Austria), following the guidelines specified in DIN EN ISO 6508-1 [20]. The pyramid shaped Vickers indenter has a 136° opening angle and applied a load of 0.1 kg at a holding time of 10 seconds. The test points were positioned equidistant at 0.15 mm from each other.

3. Results and discussion

3.1. Layer formation analysis

Analysis of deposit cross sections

The process parameters employed using an inner (AA5083) and an outer (AA2024) as well as common (only AA2024 or AA5083) stud material led to overall stable deposition behavior for all experiments. All layers deposited show a rough surface as well as unbonded parts of the deposit on advancing side and retreating side, which is process-characteristic. An exemplary cross section is shown in Fig. 2, where the FS layer is formed by inner and outer stud material. Via EDS analysis, both materials can be clearly distinguished by their main alloying elements, see Fig. 2. The distribution of inner and outer stud material within the deposit presents some general characteristics that are independent of the process parameters, as shown in Fig. 3, including the corresponding layer material segmentation. In general, five different zones in the deposits can be distinguished, *i.e.* bottom part, top part, advancing side, retreating side and center, see Fig. 3 Sample 1 and Schematic.

However, the characteristics of these different zones, see Fig. 3 Schematic, are influenced by the process parameters. For instance, a decrease of axial force results in a significantly thicker top part of the layer (Fig. 3 Sample 2) compared to high axial forces (Fig. 3 Sample 3). A similar behavior is observed for a decreased rotational speed (Fig. 3 Sample 4) as well as for a decreased travel speed (Fig. 3 Sample 6). Similar to the top, the outer stud material can be found at the bottom and on the advancing side of the deposit. However, for increasing values of axial force and rotational speed, slight mixing[2] on the advancing side can be observed (Fig. 3 Sample 3 and 5). A change of travel speed does not influence the material mixing on advancing side, Fig. 3 Samples 6 and 7. Enhanced mixing in the bottom part of the layers is observed for an increasing axial force (Fig. 3 Sample 3) and rotational speed (Fig. 3 Sample 5) as well as a decreasing travel speed (Fig. 3 Sample 6). In all layers and for all parameters, there is a strong mixing of both materials on the retreating side, while only the inner stud material is present in the center of the layers. The size of this central region increases for increasing axial force, rotational speed as well as decreasing travel speed.

The effect of process parameters on the deposit thickness and width is well known, see for instance [21,22], and no further discussion of it is included here for brevity. The results in terms of deposit geometry are presented in Table 2. In addition to the effects already known, the present study shows that the process parameters have significant effect on the ratio of inner and outer stud material in the deposited layer as well as on the distribution of the inner material within the deposited layer, *i.e.* on the layer formation.

According to Fukakusa [19], the material in the center of the stud forms the layer, whereas the peripheral material forms the flash. Therefore, the term 'contact radius', r_c, had been defined. The value of r_c describes the radius of the assumed area of the stud material that is in contact with the subjacent material and contributes to the formation of the layer. It is calculated by

$$r_c = \sqrt{\frac{A \cdot v}{\pi \cdot v_{cr}}}, \tag{1}$$

where A is the layers' cross sectional area,[3] v the travel speed and v_{cr} the stud consumption rate. Table 2 presents the resulting r_c values for

[2] No significant chemical mixing could be observed from the FS deposits' cross sections using the two-materials studs. Mixing in this context means a heterogeneous mixture, where both alloys exist in certain areas but can still be distinguished, *e.g.* by different contrasts after chemical etching or by EDS measurements, see Fig. 2.

[3] The cross sectional area A has been determined by the image segmentation performed in ImageJ, where deposit thickness t and width w were determined from the images taken via light microscope.

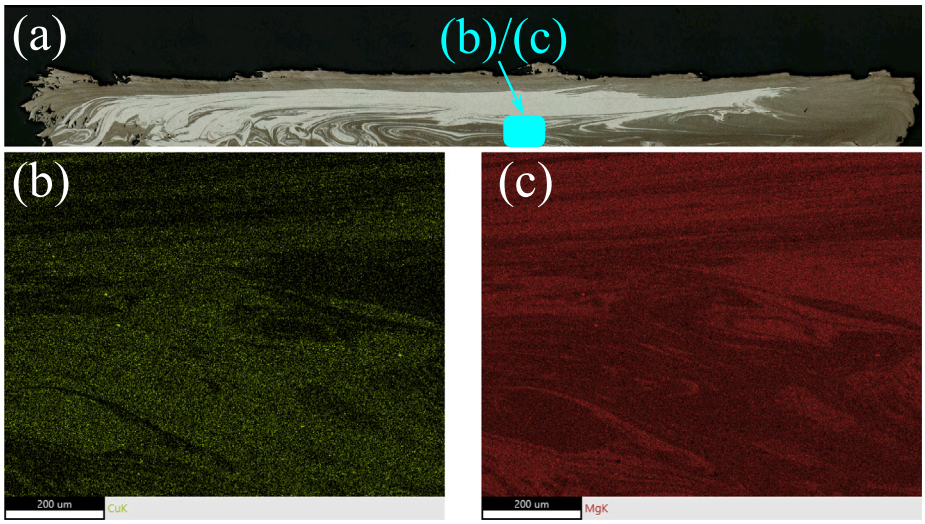

Fig. 2. Exemplary EDS scans for reference Sample 1 (a) showing the main alloying elements Cu (b) and Mg (c), indicating no chemical mixing of the two different aluminum alloys used.

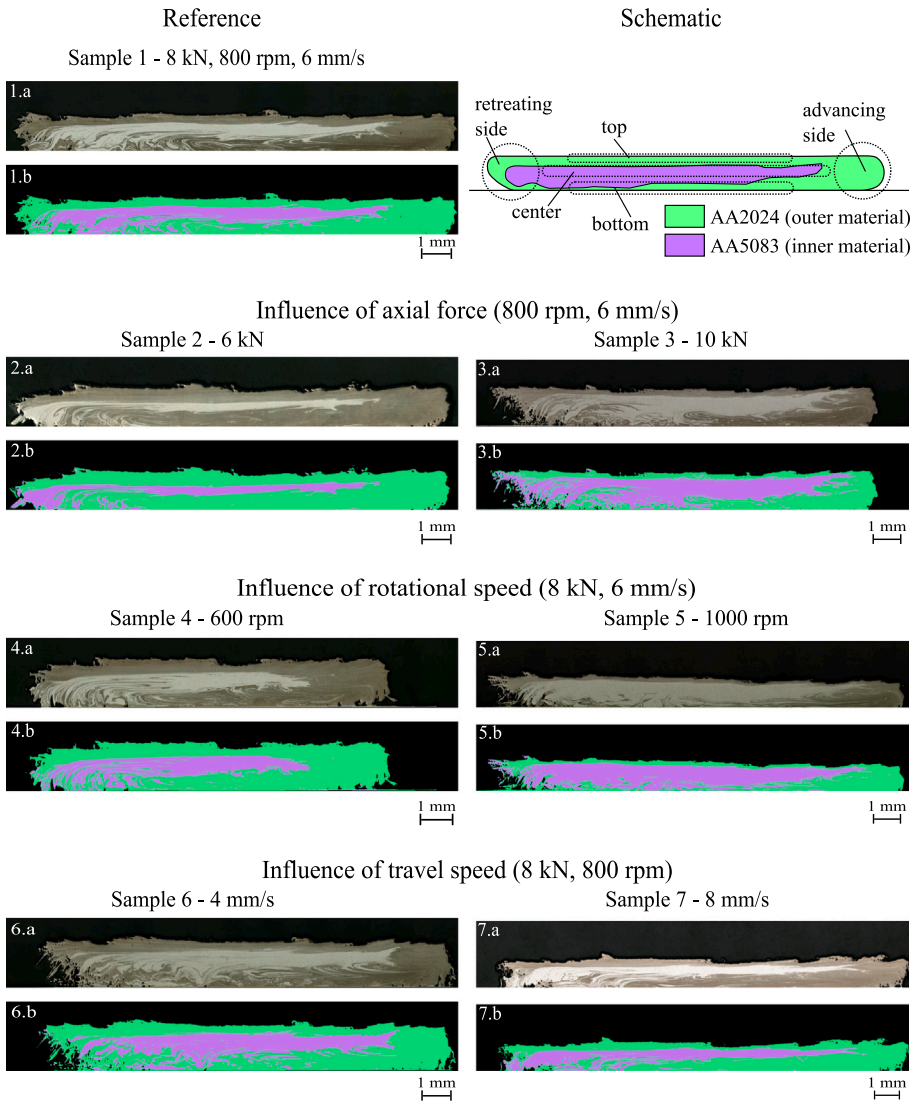

Fig. 3. Macrograph and corresponding image segmentation for FS layers deposited at different process parameters using two stud materials, *i.e.* AA2024 (outer material) and AA5083 (inner material). Overall, all layers present process-typical characteristics, *i.e.* unbonded edges on both sides and rough surfaces.

Table 2
Overview of deposit geometries, average stud consumption rate v_{cr}, assumed contact radius r_c, and percentages of inner and outer material for the processes parameters used. The sample number corresponds to the experiments listed in Table 1.

Sample	Thickness t [mm]	Width w [mm]	Area A [mm^2]	Consumption rate v_{cr} [mm/s]	Contact radius r_c [mm]	Percentage AA5083 [%]	Percentage AA2024 [%]
1	1.26	20.29	22.70	1.30	5.77	35.30	64.70
2	1.35	16.37	19.57	0.85	6.63	20.45	79.55
3	1.40	21.78	26.16	2.12	4.85	51.28	48.72
4	1.52	19.78	29.37	1.27	6.65	29.93	70.07
5	1.10	19.72	17.79	1.78	4.37	57.54	42.46
6	1.62	22.55	32.63	1.27	5.72	40.07	59.93
7	1.10	18.62	16.33	1.48	4.79	32.65	67.34
8	2.39	21.93	43.39	2.16	6.19	100	–
9	1.20	19.30	20.42	1.31	5.46	–	100
10	3.20	23.31	60.00	2.18	7.25	100	–
11	1.75	19.58	28.86	1.49	6.08	–	100
12	1.89	19.49	31.00	2.35	5.02	100	–
13	1.08	19.69	18.06	1.26	5.23	–	100

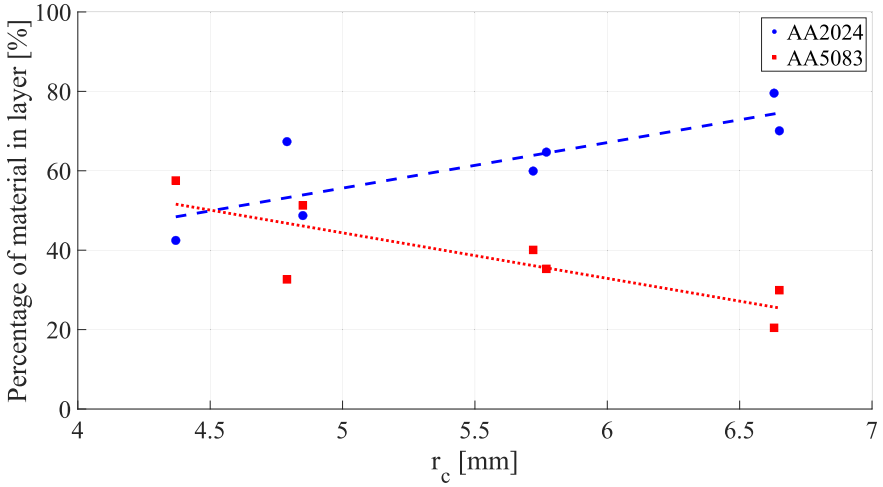

Fig. 4. The assumed contact radius r_c is in direct relation with the percentage of inner (AA5083) and outer (AA2024) stud material in the respective deposit obtained via the cross sections' image segmentation. A higher r_c value means that more outer material is within the zone that forms the deposit, represented by a higher percentage of outer stud material (AA2024).

all experiments performed as well as the ratio of inner and outer stud material in the deposit.

Fukakusa [19] stated, that r_c decreases with increasing rotational speed and axial force, which is also observed in this study. Additionally, a recent study by Agiwal et al. [23] presented that the ratio of the contact radius to the initial consumable stud radius is influenced by the tangential velocity. For higher axial forces, the stud consumption rate v_{cr} increases faster than the area of the layer, resulting in lower r_c values. For higher rotational speeds, the layer area decreases whereas the stud consumption increases, which both lead to lower r_c values. Considering the special stud design used in this study for the visualization of the FS layer formation, a larger contact radius means that more outer material is within the zone that forms the deposit, represented by a higher percentage of outer stud material (AA2024), see for instance Fig. 3 (Sample 2). On the other hand, a smaller contact radius leads to the fact that mainly inner material is within the contact area forming the deposit, see for instance Fig. 3 (Sample 3). Fig. 4 shows this trend and summarizes all r_c values and the corresponding layer percentages.

The FS deposition behavior, for instance, considering the deposit thickness and feed rate, for the special purpose two-materials studs (inner and outer stud material) used in this study is more similar to the respective AA2024 (common) studs than for AA5083 (common) studs, Table 2, where the common studs are machined from one single material only. Due to the fact that the AA2024 alloy presents a higher strength at the FS process temperatures and since the consumable two-materials stud consists of a higher percentage of AA2024 than AA5083, the AA2024 alloy significantly affects the feed rate of the two-materials studs, *i.e.* the two-materials studs' feed rates tend to be lower than AA5083 feed rates. The comparison to the respective reference depositions that have been performed with common studs made of one single material presents an overall similar behavior and, therefore, the two-materials stud are a reasonable approach to visualize the FS layer formation.

Analysis of stop action experiments

In the following, the samples taken from the stop action experiments are investigated in order to analyze the layer formation in the FS process when the stud is still in contact with the deposit. Cross sections, Fig. 5, and longitudinal sections, Fig. 6, were taken at different radial positions of the stud for Sample 1, see Table 1. The investigation of multiple positions within the stop action samples allows a continuous analysis of the transfer of inner/outer stud material into the layer or into the flash, respectively, *i.e.* a detailed understanding of the material flow behavior during processing.

Fig. 5 (C.1) refers to a cross section at the rear edge of the stud in a steady processing state, whereas (C.3) is close to the center and (C.4) is the cross section at the front of the stud during the layer formation. In this regard, Fig. 5 (C.1) represents the complete deposition, where Fig. 5 (C.2 to C.4) show stages in terms of material flow during layer formation. The outer stud material is deposited on the advancing side

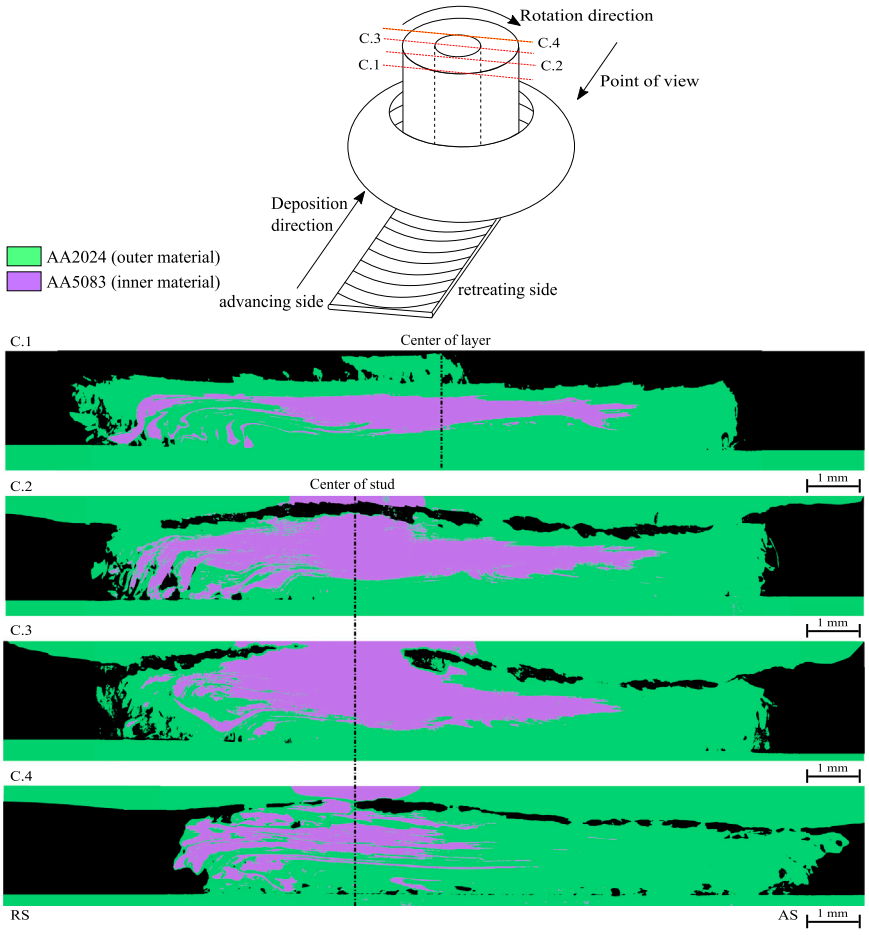

Fig. 5. Cross sections taken from stop action experiment of Sample 1, at different positions along the stud. AA2024 represents the outer material and AA5083 the inner stud material.

and the bottom of the layer, whereas mixing of inner and outer stud material occurs mainly on the retreating side. In the center, the region of inner material is thicker near the center position of the stud, (C.2, C.3) in Fig. 5, as compared to the final layer (C.1). Furthermore, for the cross-sections near the center of the stud, the material at the top consists mainly of the inner stud material as it is flowing directly from the inner part of the stud in the deposited shear layer. A significant difference between Fig. 5 (C.2, C.3 and C.4) is also the state of the layer formation on the retreating side. As can be seen from Fig. 5 (C.4), the advancing side is formed first in front of the stud, whereas the retreating side gradually forms towards the rear edge of the stud. The observed material flow from advancing side to retreating side is in agreement with findings reported by other studies [16,24]. The flow of the material during the stud rotation from retreating side towards advancing side at the rear edge of the stud is restricted by the already deposited material, resulting in the deposit formation on the retreating side. This results in two characteristic phenomena of the FS process. Firstly, an offset between the center of the stud, Fig. 5 (C.2 to C.4), and the center of the final layer, Fig. 5 (C.1). The layer is shifted towards the advancing side, as discussed in literature extensively, see for instance Gandra et al. [25]. Secondly, the material on the retreating side experiences consolidation towards the substrate for a shorter amount of time compared to the advancing side, leading to more pronounced unbonded edge regions, see retreating side in Fig. 5 (C.1). This can also be observed in front of the stud, Fig. 5 (C.4), as the layer did not yet experience compression towards the substrate by the stud above, leading to initially significant bonding defects. Additionally, a superficial layer of outer stud material forms on the top, which can be observed at the rear of the stud material, Fig. 5 (C.1).

The corresponding longitudinal sections of the stop action experiment are shown in Fig. 6. On the advancing side, Fig. 6 (L.1), mainly outer stud material (AA2024) is present which seems to be a fundamental phenomenon as previously discussed. The nature of the FS deposition process, namely the rotational and translational movement, hinders the inner stud material to flow from retreating side or center towards the advancing side in front of the stud's axis of rotation. The section in Fig. 6 (L.2) is closer to the center and more inner stud material is present in the layer, where there are also some thin material flow lines pointing downwards. A low degree of mixing of inner and outer stud material can be observed. Fig. 6 (L.3 to L.5) present the longitudinal sections $\pm$ 2 mm from the center of the stud. It is clearly indicated that the inner stud material forms the center of the deposited layer. At the bottom, mainly outer material is present, but in the region close to the center of the stud, areas mixed of inner and outer stud material exist, Fig. 6 (L.4). In front of the rotational axis of the stud, the material flows down towards the substrate surface, where the layer material is not yet completely bonded to the substrate, Fig. 6 (L.3b). Below the center of the stud, mainly inner stud material is forming the layer. However, the bottom region of the layer is formed by outer material, which is flowing in front of the studs' rotational axis from the advancing side towards the center during the rotational and translational movement of the stud. Behind the centerline of the stud, the top part of the layer is formed, consisting of outer material, Fig. 6 (L.3a), which has been identified as fundamental characteristic for this deposition process in the discussion above. From the stop action experiment, it can be observed that this top part of the FS deposit is formed at the rear edge of the stud. The longitudinal sections Fig. 6 (L.5 and L.6), which are at the retreating side, present a mixture of inner

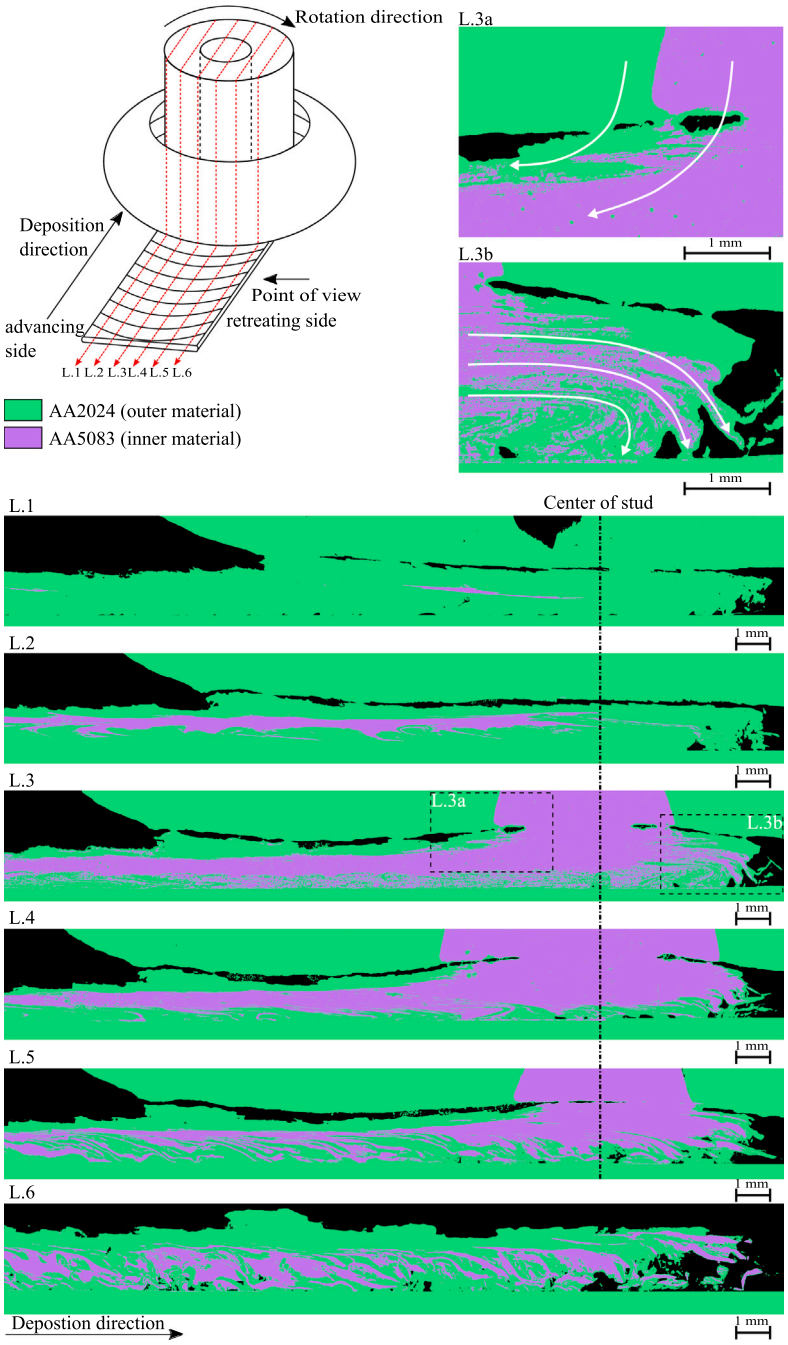

Fig. 6. Longitudinal sections taken from stop action experiment of Sample 1, at different positions along the stud. AA2024 represents the outer material and AA5083 the inner stud material.

and outer stud material in almost the whole layer formed. An exception is the top part of the layer consisting of outer stud material only.

Overall, the stop action experiments present a characteristic flow and layer formation behavior similar to the observation from the cross sections presented in Fig. 3 in terms of inner and outer stud material distribution within the final layer. Additionally, an insight into the layer formation and distribution of inner and outer stud material below the stud could be gained. The inner stud material forms the center of the layer and is also present at the bottom and on the retreating side, where it is mixed with outer stud material. The advancing side is mainly formed by outer stud material similar to the top part, where the latter was observed to be formed at the rear edge of the stud during the FS deposition process. The special stud configuration of the present study enabled the visualization of FS-characteristic layer formation patterns of aluminum alloys, however, it is assumed that the results are directly transferable to the layer formation using common (single material) studs. This assumption is based on the observation that the same layer formation behaviors were obtained for different special consumable studs made of different aluminum alloy combinations, see Appendix A. Therefore, experiments performed with only one stud material (Samples 8 and 9) are selected for the in-depth microstructure analysis in the following.

3.2. Correlation of microstructure with layer formation

For the analysis of the microstructure, five positions in regions that showed significant differences in layer formation were selected, *i.e.* advancing side, top, center, bottom and retreating side. The layers

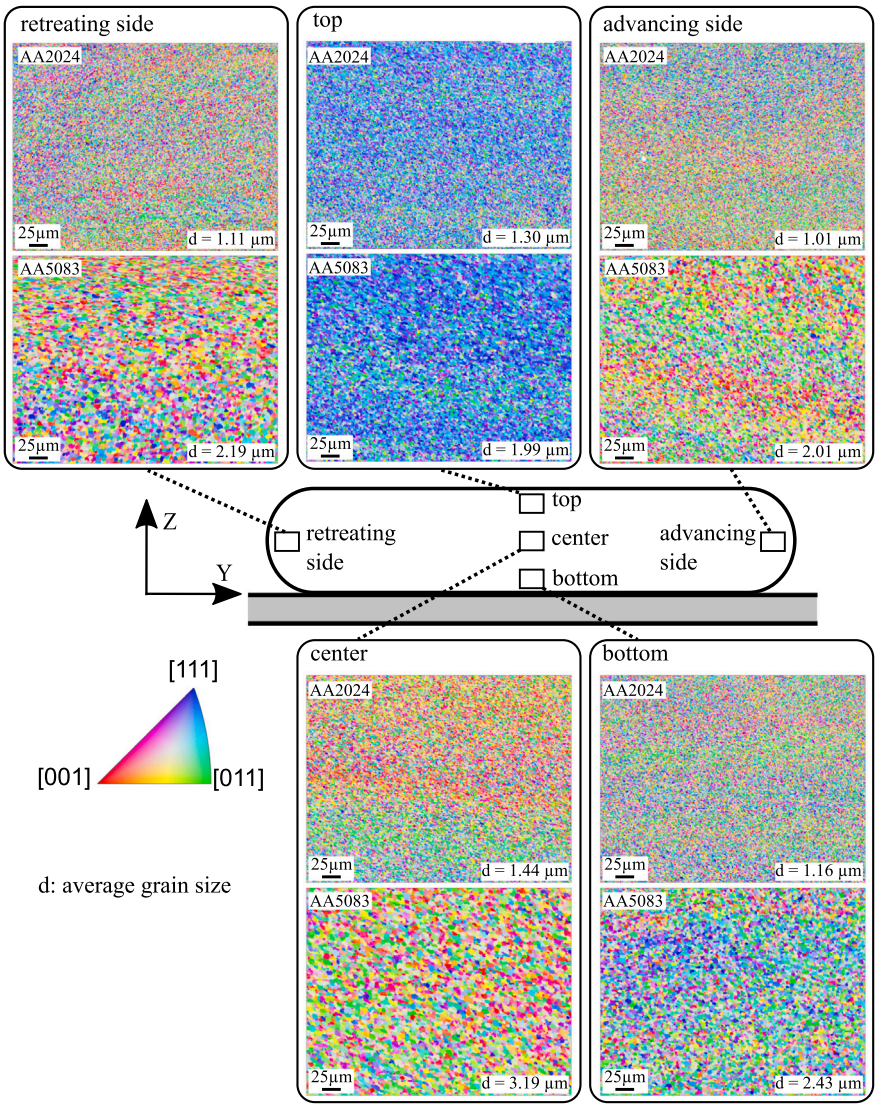

Fig. 7. Inverse pole figure maps of samples 8 (AA5083) and 9 (AA2024) in all scanned regions.

for this investigation were deposited with studs containing only one material, *i.e.* AA2024 or AA5083, respectively. The scans in the top region, the advancing side and the retreating side were performed at the edge of the layer, the bottom region was scanned directly above the layer-to-substrate interface. The inverse pole figure maps of similar process parameters for both alloys (Samples 8 and 9, Table 1) are displayed in Fig. 7. In all investigated regions, an equiaxed grain morphology is observable, see Appendix B. As already known from previous studies [11,13,14], the grain size within the layer presents slight gradients, which can be directly related to the above mentioned layer formation phenomena. The average grain size in the center of the layers is the largest, *i.e.* 1.44 ± 0.66 µm (AA2024) and 3.19 ± 1.97 µm (AA5083). It decreases towards the other regions of the layers. In the layer formation analysis, those regions mainly or only contained outer stud material. There are different aspects influencing the grain size after plastic deformation and recrystallization. Temperatures and cooling rates during processing affect the resulting microstructure. For instance, Rahmati et al. [11] found smaller grains at the bottom of the layers due to higher heat dissipation into the substrate. Additionally, the strain rate is another important factor, which is approached via numerical models [26,27] as it can hardly be assessed via experimental investigations. The two-materials stud configuration used in this study allows the qualitative visualization of the relation between position of the respective material in the stud and within the deposit. The greater the distance of the radial position from the studs rotation axis, the higher the tangential velocity and the higher the strain rate [23]. Therefore, the material in the center of the stud, which mainly forms the layer's center, experiences a lower strain rate and consequently strain, resulting in the slightly larger grains in this part of the layer. The correlation between layer formation, expected strain rates and resulting grain sizes confirms the results of a previous study that found smaller grains at the interfaces and larger grains in the center of the layer within a multi-layer FS stack [13]. Furthermore, it also gives an explanation for the observation of smaller grains on advancing side and retreating side compared to the center reported in the investigation of Ehrich et al. [14].

For non-precipitation hardenable aluminum alloys like AA5083, the grain size is in direct relation with the hardness. Consequently, the slight gradients in terms of grain size within a FS deposit lead to gradients in hardness presented along multi-layer FS build direction, *i.e.* layers' thickness in a previous study [13] and in detail for Sample 8 in Fig.C.1(b). As already known from the literature, additional phenomena occur for precipitation hardenable alloys and the evolving hardness distribution is more complex as it is not only determined by the grain size, see for instance Appendix C. As the relation between microstructure and hardness has already been presented, no further

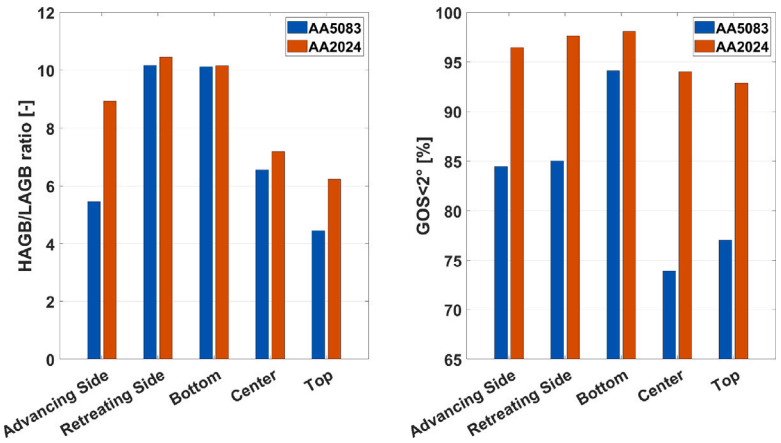

Fig. 8. Analysis of the degree of recrystallization by HAGB/LAGB ratio and GOS criteriafor Samples 8 and 9 (common studs containing one single material only).

discussion is included in this study for brevity. However, the interested reader is referred to a previous study by the authors [13].

Besides the different grain sizes within the FS deposit, there is a significant difference in texture between the top region and the other regions. Whereas the majority of the regions investigated shows random texture characteristics, a shear-dominant texture ($B\{\bar{1}12\}\langle 110\rangle/\bar{B}\{1\bar{1}\bar{2}\}\langle\bar{1}\bar{1}0\rangle$ texture components [28]) can be observed in the top part of the deposit for both Al alloys used, Fig. 7, as often reported for friction stir welding processes of face centered cubic materials [29]. Since the top part of the layer is formed at the rear edge of the stud, as shown in Figs. 5 and 6, different deposition mechanisms seem to prevail. The layer deposition via the FS principle relies on the formation of a shearing interface below the rotating consumable stud. The outer parts of the consumable stud material form the process-characteristic flash and the material in the assumed contact area is deposited by shearing off from the stud tip at the shearing interface. In front of the stud, the material flows towards the substrate forming the main part of the deposit, Fig. 6. During this part of the layer formation, the material undergoes severe plastic deformation causing dynamic recrystallization, which results in a fine equiaxed grain structure with a random texture. The conditions for the FS layer formation are different in front of the stud and at its rear edge. At the rear edge, the material that has already been deposited in front of the studs rotational axis is present and experiences further consolidation. The material at the rear edge of the stud is sheared off the stud and consequently undergoes severe plastic deformation, forming the top part of the final deposit. In this regard, the resulting microstructure of the top part of the deposit presents a texture dominated by $B\{\bar{1}12\}\langle 110\rangle/\bar{B}\{1\bar{1}\bar{2}\}\langle\bar{1}\bar{1}0\rangle$ shear components. Compared to the material deposited in the front, the rear edge material interacts with previously deposited part of the layer, *i.e.* shears off, and does not experiences further consolidation as the translational movement continues. The top part shows a reduced degree of recrystallization compared to the parts of the layer below, as shown by two different criteria, *i.e.* ratio of HAGB to LAGB and grain orientation spread (GOS) in Fig. 8. The induced plastic deformation consequently weakens the texture to a certain extent depending on the selected parameter. The change of process parameters, which influence the contact radius, is assumed to affect the texture especially in the top part of the layer in a similar way as observed for the thickness of the top part, Fig. 3. Using the example of the change in rotational speed, the influence on the microstructure with focus on the texture in the top part of the layer is examined in more detail in the following.

In the literature, the influence of rotational speed has been investigated in experimental and numerical studies. The rotational speed was found to affect the material flow from consumable stud into the top part of the deposit [16]. With regard to the microstructure, Rahmati et al. [11] stated that an increased rotational speed leads to coarser grains for AA2024 deposits over AA1050 substrates. This is in agreement with Aval [30], who found that a minimum grain size could be observed for low rotational speeds as well as low axial feed rates for the deposition of AA6061. However, the EBSD measurements in this study, did not reveal a clear trend for rotational speed and grain size. The top regions of the respective AA2024 and AA5083 layers, do not present a significant difference in terms of grain size, Fig. 9.

However, the rotational speed influences the texture evolution for the top region of the AA2024 and AA5083 layers, as shown in Fig. 9 by means of inverse pole figure map and pole figure. The pole figures for the lowest rotational speed, *i.e.* 600 rpm, show the highest texture intensity with a dominance of $B\{\bar{1}12\}\langle 110\rangle/\bar{B}\{1\bar{1}\bar{2}\}\langle\bar{1}\bar{1}0\rangle$ texture components [28]. For both alloys, the texture intensity is decreasing with an increase of rotational speed, indicating a less pronounced shear deformation. Similar findings were reported by Yu et al. [12] and Rahmati et al. [31], analyzing the texture in the center of the layers, for AA6061 layers on Q235 substrates and for AA2024 deposits on AA1050 substrates, respectively. In the present study, however, the microstructural analyses in the center of all layers showed no dominant textural component, indicating that only in the top part of the layer, larger amounts of shear strain were introduced to the material during the process. By increasing the rotational speed, the process temperature increases [32] and the deposited material experiences more plastic deformation. Furthermore, for a force-controlled process, keeping the axial force constant at 8 kN, the lower radius of the assumed contact area leads to a higher pressure where the material is sheared off. These effects lead to a higher strain, which enhances dynamic recrystallization during the deposition process. As a result, the texture intensity decreases.

Besides the change of texture intensity, the thickness of the area presenting shear texture depends on rotational speed as well. The inverse pole figure maps in Fig. 10 represent scans from the top of the layer towards the center from right to left for AA5083 layers that were analyzed regarding their texture in 100 μm segments. For an increasing rotational speed, the thickness of the textured area decreases. This observation correlates with the results from the layer formation analysis, as for higher rotational speeds the top part of the layer formed by the outer stud material decreases in thickness as well.

At a lower rotational speed, the radius of the assumed contact area increases, Table 2, and therefore a larger amount of material is sheared off the stud tip at the rear edge of the consumable stud. Hence, more material is deposited from the outer area of the stud, *i.e.* at higher r_c values. As a result, the shear textured area is thicker at lower rotational speeds.

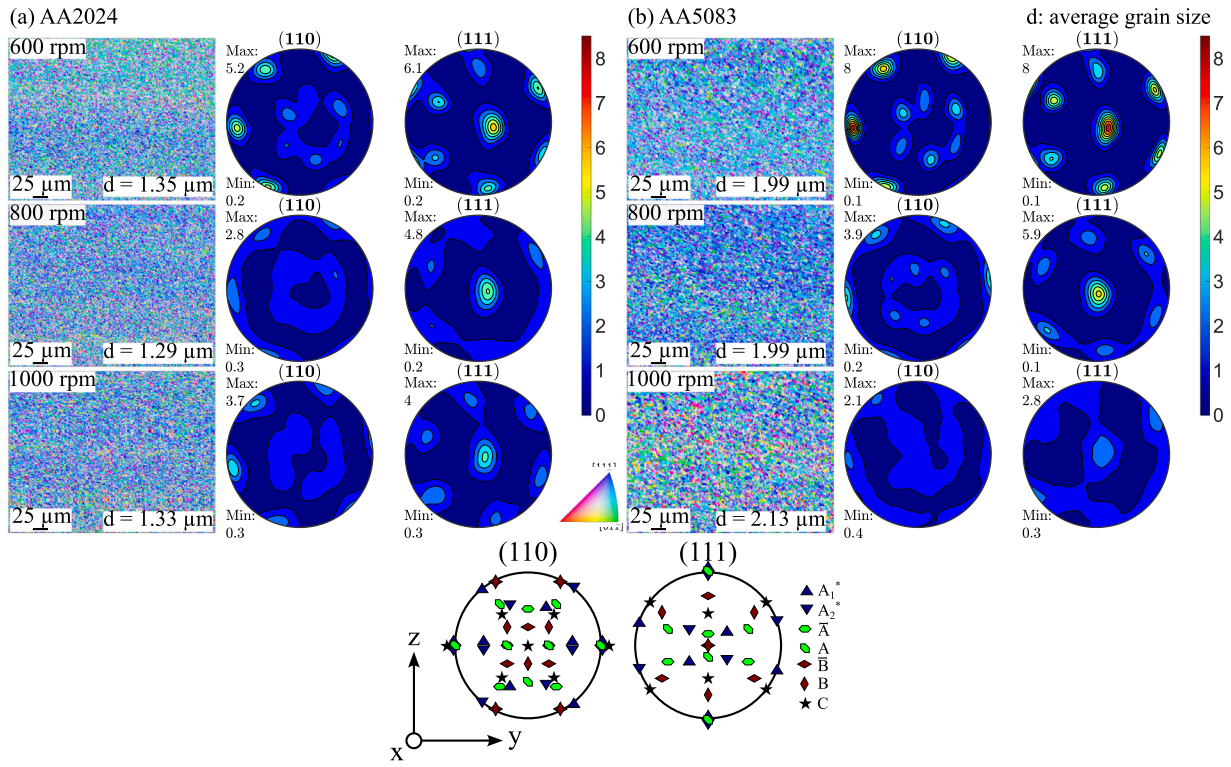

Fig. 9. Influence of rotational speed on the texture evolution in the top part of the layers. The projections of ideal shear texture components for face-centered cubic metals are displayed in the (110) and (111) pole figures below [33].

4. Conclusions

The study presents an insight into the layer formation during FS deposition and investigated the influence of layer formation on microstructural properties. The analysis was performed using a special stud configuration with different inner (AA5083) and outer (AA2024) stud materials, to visualize how the two materials contribute to the formation of different parts of the deposit. Additionally, common studs of AA2024 and AA5083 were used for validation of the respective mechanisms by microstructure analysis. In contrast to other material flow approaches, the special stud configuration in combination with in-depth analyses from stop action experiments allowed an unprecedented insight into the FS layer formation. The main findings can be summarized as follows:

- A characteristic layer formation pattern can be observed independent of the selected process parameters. Only material of the outer periphery of the stud is located in the top region and the advancing side of the layer. The inner material is deposited in the center of the layer. Material mixing, but no chemical mixing, of both materials occurs on the retreating side and slightly in the bottom region.
- The FS process parameters have significant effect on the ratio and distribution of inner and outer stud material in the deposited layer. A higher percentage of inner material is deposited for increased values of axial force and rotational speed as well as for decreased travel speeds.
- The top region of the layer is formed at the rear edge of the stud from retreating side towards the advancing side.
- The smallest average grain sizes are observed in the regions of the layer where mainly outer stud material is deposited. Thus, largest grain sizes are observed in the layers' center. This characteristic might be related to the process strain rates, as material from the outer part of the stud experiences higher strain rates leading to smaller grains.
- A pronounced texture was only observed in the top region of the deposits, where texture components ($B\{\bar{1}12\}\langle 110\rangle/\bar{B}\{1\bar{1}\bar{2}\}\langle\bar{1}\bar{1}0\rangle$) indicate shear texture. The texture in this part of the deposit can be related to the layer formation mechanism, *i.e.* the top part is formed at the rear edge of the stud, where the material flow conditions differ compared to in front of the stud. The intensity as well as the thickness of the textured areas decrease with increasing rotational speeds.

Funding

This project has received funding from the European Research Council (ERC) under the European Unions Horizon 2020 research and innovation programme (Grant Agreement No. 101001567).

CRediT authorship contribution statement

Marius Hoffmann: Writing – review & editing, Writing – original draft, Visualization, Validation, Methodology, Investigation, Formal analysis, Data curation, Conceptualization. **Zina Kallien:** Writing – review & editing, Writing – original draft, Visualization, Validation, Methodology, Investigation, Formal analysis, Data curation, Conceptualization. **Eduardo Antunes Duda:** Writing – review & editing, Visualization, Investigation. **Benjamin Klusemann:** Writing – review & editing, Supervision, Resources, Funding acquisition.

Declaration of competing interest

The authors declare that they have no known competing financial interests or personal relationships that could have appeared to influence the work reported in this paper.

Data availability

The obtained data of this research is online available at Zenodo (https://doi.org/10.5281/zenodo.13734042).

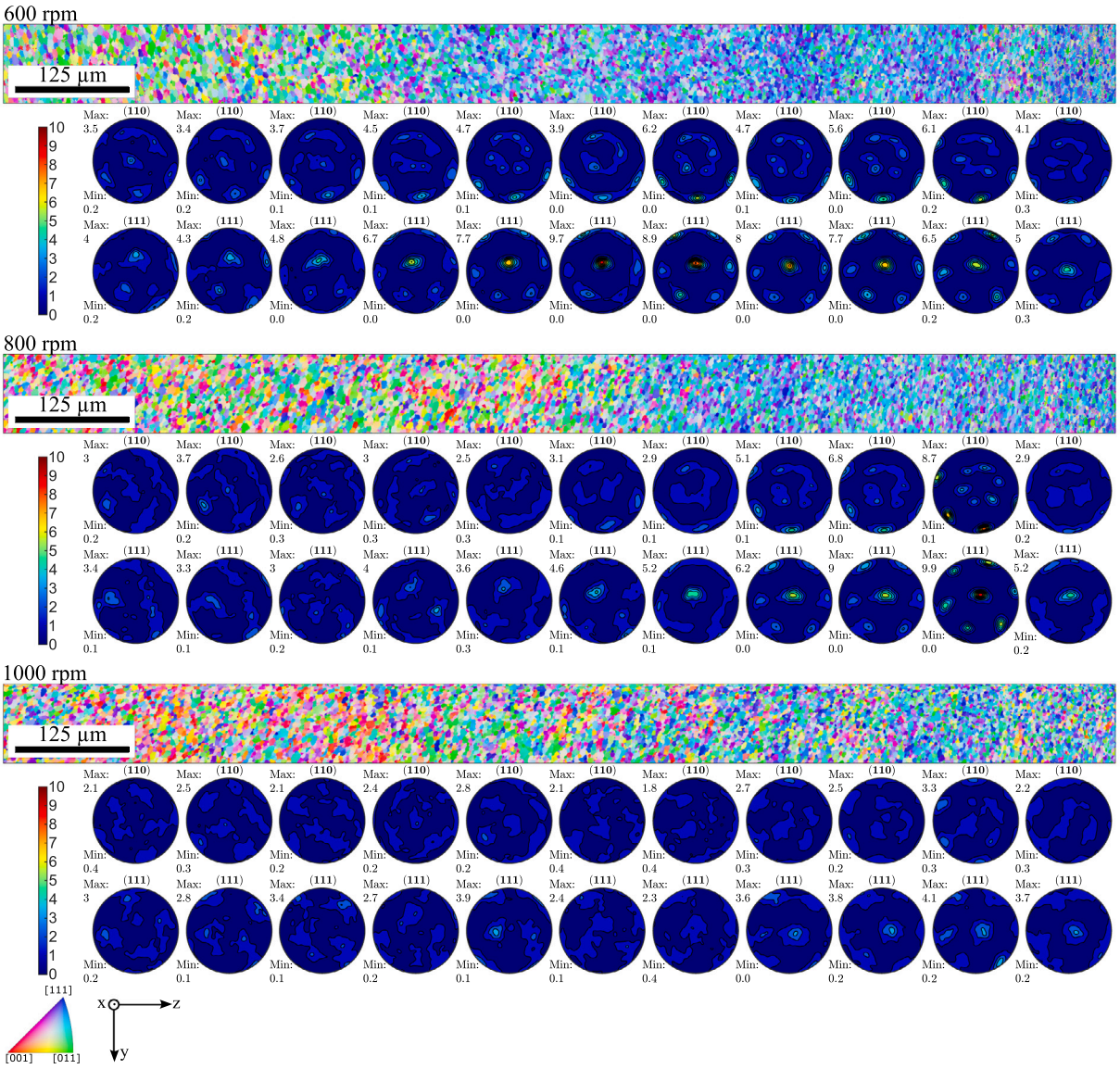

Fig. 10. Influence of rotational speed on texture and shear layer thickness in the top part of the AA5083 layers. The scans were divided into segments of 100 µm length for the analysis. The right side of the inverse pole figure maps corresponds to the top of the layers, the left side is the central region of the layer.

Appendix A. Layer formation analysis using different stud material combinations

In order to show that the layer formation phenomena observed with AA2024/AA5083 special consumable studs are valid for different material combinations, tests were carried out with reverse inner and outer stud material, *i.e.* AA5083 as outer and AA2024 as inner stud material, where all dimensions were kept constant. One exemplary cross section is shown in Fig. A.11. Overall, similar observations were made, see Fig. 3, which indicates that the observed layer formation characteristic is a general phenomenon for FS layer deposition.

Appendix B. Chord length distribution

The directional resolved chord length distribution (CLD) of the grains was determined based on the work of Latypov et al. [34] using their free MATLAB code 'calc_CLD' at an angle resolution of 1°. All EBSD scans performed in this study obtained an equiaxed grain morphology as illustrated in Fig. B.1.

Appendix C. Correlation of hardness with layer formation

To correlate the layers' local mechanical properties in terms of hardness with the layer formation, the samples 8 (AA5083) and 9 (AA2024) were chosen for analysis of the hardness distribution, Fig. C.1.

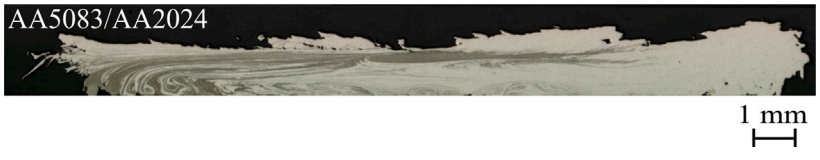

Fig. A.11. Macrograph for FS layer deposited with reversed stud materials, *i.e.* AA5083 (outer material) and AA2024 (inner material) at 6 kN, 800 rpm and 6 mm/s.

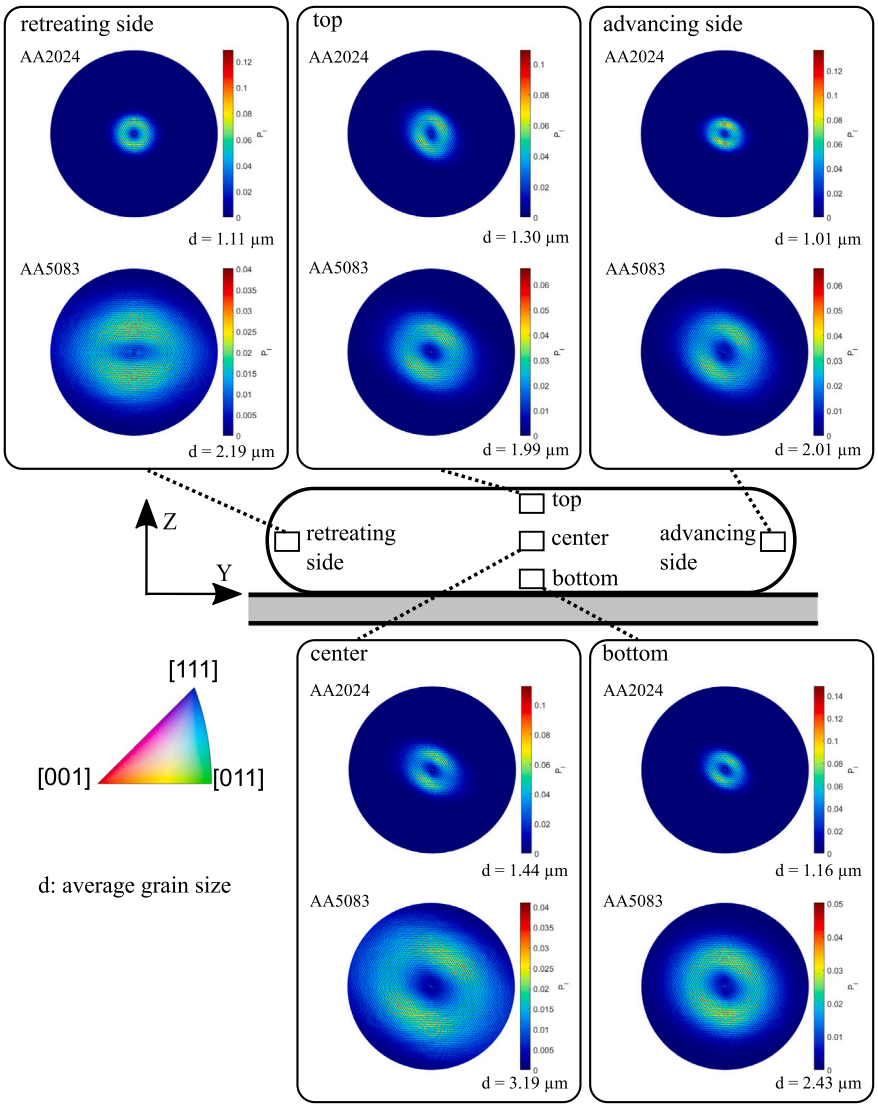

Fig. B.1. CLD maps of samples 8 (AA5083) and 9 (AA2024) in all scanned regions.

Being among the non-precipitation hardenable aluminum alloys, the grain size is one major aspect determining the strength of AA5083. The hardness distribution of the AA5083 deposit, Fig. C.1(a), presents a hardness, which is in the range of the base material (93 ± 6 HV0.1). However, slight gradients are observable within the layer, where slightly higher values can be observed on the advancing side and in the top part, *i.e.* 93.5 ± 0.3 HV0.1 (advancing side) and 91.0 ± 0.4 HV0.1 (top), respectively. The rest of the layer presents a slightly lower hardness of 84.9 ± 0.9 HV0.1, which results in a hardness difference between advancing side and retreating side of 7.6% for AA5083 (Sample 8). Overall, the regions of slightly higher hardness are in good agreement with the regions, where smaller grains have been detected, for AA5083. This phenomenon can be related to the Hall–Petch strengthening effect [35] which plays a major role for this alloy, which was also observed for MLFS structures along build direction [13].

In contrast, AA2024 is a precipitation hardenable alloy and the characteristic hardness distribution of the FS deposit shows a different appearance, Fig. C.1(b). The hardness difference between advancing side and retreating side is less pronounced for AA2024 (1.5%) and the layer rather shows a continuous decrease in hardness from top

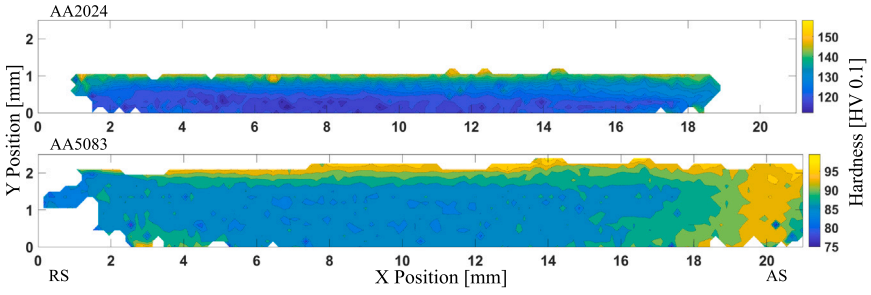

Fig. C.1. Hardness distribution of samples 9 (AA2024) (a) and 8 (AA5083) (b).

(138.0 ± 1.7 HV0.1) to bottom (121.0 ± 1.0 HV0.1), which was noticed for FS/MLFS of precipitation hardenable aluminum alloys before [13, 36]. The precipitation hardening is one major strengthening mechanism for AA2024 and since the top part of the layer is formed at the rear edge of the consumable stud, Fig. 6, it experiences the process temperature over a shorter period of time compared to the material that is deposited at the front, which might cause less overageing.

Overall, the non-precipitation hardenable AA5083 presents a clear relation between the local microstructure that evolved due to the FS layer formation and the hardness. For AA2024, the additional aspect of precipitates has a more pronounced effect on the resulting hardness distribution compared to local microstructural gradients.

References

[1] O. Abdulhameed, A. Al-Ahmari, W. Ameen, S.H. Mian, Additive manufacturing: Challenges, trends, and applications, Adv. Mech. Eng. 11 (2) (2019) 1687814018822880, http://dx.doi.org/10.1177/1687814018822880.

[2] J. Bai, H. Ding, J. Gu, X. Wang, H. Qiu, Porosity evolution in additively manufactured aluminium alloy during high temperature exposure, in: IOP Conference Series: Mater. Sci.Eng., 167, IOP Publishing, 2017, 012045, http://dx.doi.org/10.1088/1757-899X/167/1/012045.

[3] E. Cicală, G. Duffet, H. Andrzejewski, D. Grevey, S. Ignat, Hot cracking in Al-Mg-Si alloy laser welding - operating parameters and their effects, Mater. Sci. Eng. A 395 (1–2) (2005) 1–9, http://dx.doi.org/10.1016/j.msea.2004.11.026.

[4] C. Li, Z. Liu, X. Fang, Y. Guo, Residual stress in metal additive manufacturing, Procedia Cirp 71 (2018) 348–353, http://dx.doi.org/10.1016/j.procir.2018.05.039.

[5] W.E. Frazier, Metal additive manufacturing: A review, J. Mater. Eng. Perf. 23 (6) (2014) 1917–1928, http://dx.doi.org/10.1007/s11665-014-0958-z.

[6] R.S. Mishra, R.S. Haridas, P. Agrawal, Friction stir-based additive manufacturing, Sci. Technol. Weld. Join. 27 (3) (2022) 141–165, http://dx.doi.org/10.1080/13621718.2022.2027663.

[7] J. Dilip, G.D. Janaki Ram, Microstructure evolution in aluminum alloy AA 2014 during multi-layer friction deposition, Mater. Charact. 86 (2013) 146–151, http://dx.doi.org/10.1016/j.matchar.2013.10.009.

[8] M. Soujon, Z. Kallien, A. Roos, B. Zeller-Plumhoff, B. Klusemann, Fundamental study of multi-track friction surfacing deposits for dissimilar aluminum alloys with application to additive manufacturing, Mater. Des. 219 (5) (2022) 110786, http://dx.doi.org/10.1016/j.matdes.2022.110786.

[9] L. Rath, Z. Kallien, A. Roos, J.F. d. Santos, B. Klusemann, Anisotropy and mechanical properties of dissimilar al additive manufactured structures generated by multi-layer friction surfacing, Int. J. Adv. Manuf. Technol. 117 (6) (2023) 371, http://dx.doi.org/10.1007/s00170-022-10685-3.

[10] U. Suhuddin, S. Mironov, H. Krohn, M. Beyer, J.F. Dos Santos, Microstructural evolution during friction surfacing of dissimilar aluminum alloys, Metall. Mater. Trans. A 43 (13) (2012) 5224–5231, http://dx.doi.org/10.1007/s11661-012-1345-8.

[11] Z. Rahmati, H. Jamshidi Aval, S. Nourouzi, R. Jamaati, Effect of friction surfacing parameters on microstructure and mechanical properties of solid-solutionized AA2024 aluminium alloy cladded on AA1050, Mater. Chem. Phys. 269 (2021) 124756, http://dx.doi.org/10.1016/j.matchemphys.2021.124756.

[12] M. Yu, H. Zhao, Z. Zhang, L. Zhou, X. Song, N. Ma, Texture evolution and corrosion behavior of the AA6061 coating deposited by friction surfacing, J. Mater. Process. Technol. 291 (2020) 117005, http://dx.doi.org/10.1016/j.jmatprotec.2020.117005.

[13] Z. Kallien, M. Hoffmann, A. Roos, B. Klusemann, Correlation of microstructure and local mechanical properties along build direction for multi-layer friction surfacing of aluminum alloys, JOM (2023) http://dx.doi.org/10.1007/s11837-023-06046-4.

[14] J. Ehrich, A. Roos, B. Klusemann, S. Hanke, Influence of Mg content in Al alloys on processing characteristics and dynamically recrystallized microstructure of friction surfacing deposits, Mater. Sci. Eng. A 819 (2021) 141407, http://dx.doi.org/10.1016/j.msea.2021.141407.

[15] C. Belei, V. Fitseva, J.F. Dos Santos, N.G. Alcântara, S. Hanke, TiC particle reinforced Ti-6Al-4V friction surfacing coatings, Surf. Coat. Technol. 329 (2017) 163–173, http://dx.doi.org/10.1016/j.surfcoat.2017.09.050.

[16] H. Khalid Rafi, G. Phanikumar, K. Prasad Rao, Material flow visualization during friction surfacing, Metall. Mater. Trans. A 42 (2011) 937–939, http://dx.doi.org/10.1007/s11661-011-0614-2.

[17] A. Deshpande, H. Agiwal, C. Baumann, S. Krall, F. Bleicher, F.E. Pfefferkorn, Recycling metal cutting chips into a consolidated deposition with friction surfacing, Manuf. Lett. 35 (2023) 743–749, http://dx.doi.org/10.1016/j.mfglet.2023.08.093.

[18] N. Gotawala, H.Z. Yu, Material flow path and extreme thermomechanical processing history during additive friction stir deposition, J. Manuf. Process. 101 (8) (2023) 114–127, http://dx.doi.org/10.1016/j.jmapro.2023.05.095.

[19] K. Fukakusa, On the characteristics of the rotational contact plane – A fundamental study of friction surfacing, Weld. Int. 10 (7) (1996) 524–529, http://dx.doi.org/10.1080/09507119609549043.

[20] M.W. nach Vickers—Teil, 1: Prüfverfahren; din en iso 6507-1: 2018-07; deutsche fassung EN iso 6507-1: 2018, 2018.

[21] J. Gandra, H. Krohn, R.M. Miranda, P. Vilaça, L. Quintino, J.F. Dos Santos, Friction surfacing—A review, J. Mater. Process. Technol. 214 (5) (2014) 1062–1093, http://dx.doi.org/10.1016/j.jmatprotec.2013.12.008.

[22] E. Seidi, S.F. Miller, B.E. Carlson, Friction surfacing deposition by consumable tools, J. Manuf. Sci. Eng. 143 (12) (2021) 031012, http://dx.doi.org/10.1115/1.4050924.

[23] H. Agiwal, H. Yeom, K. Sridharan, S. Rudraraju, F.E. Pfefferkorn, Radius of contact during friction surfacing of stainless steel 304L: Effect of spindle speed and rod diameter, J. Manuf. Sci. Eng. 146 (2) (2024).

[24] H. Khalid Rafi, K. Balasubramaniam, G. Phanikumar, K. Prasad Rao, Thermal profiling using infrared thermography in friction surfacing, Metall. Mater. Trans. A 42 (2011) 3425–3429, http://dx.doi.org/10.1007/s11661-011-0750-8.

[25] J. Gandra, D. Pereira, R.M. Miranda, R. Silva, P. Vilaça, Deposition of AA6082-T6 over AA2024-T3 by friction surfacing - mechanical and wear characterization, Surf. Coat. Technol. 223 (2013) 32–40, http://dx.doi.org/10.1016/j.surfcoat.2013.02.023.

[26] P. Pirhayati, H.J. Aval, An investigation on thermo-mechanical and microstructural issues in friction surfacing of Al–Cu aluminum alloys, Mater. Res. Express 6 (5) (2019) http://dx.doi.org/10.1088/2053-1591/ab0635.

[27] S.M. Bararpour, H.J. Aval, R. Jamaati, Modeling and experimental investigation on friction surfacing of aluminum alloys, J. Alloys Compd. 805 (2019) 57–68, http://dx.doi.org/10.1016/j.jallcom.2019.07.010.

[28] L. Tóth, K. Neale, J. Jonas, Stress response and persistence characteristics of the ideal orientations of shear textures, Acta Metall. 37 (8) (1989) 2197–2210, http://dx.doi.org/10.1016/0001-6160(89)90145-4.

[29] R.W. Fonda, K.E. Knipling, Texture development in friction stir welds, Sci. Technol. Weld. Join. 16 (2011) 288–294, http://dx.doi.org/10.1179/1362171811Y.0000000010.

[30] H. Jamshidi Aval, Comprehensive thermo-mechanical simulation of friction surfacing of aluminum alloys using smoothed particle hydrodynamics method, Surf. Coat. Technol. 419 (2019) (2021) 127274, http://dx.doi.org/10.1016/j.surfcoat.2021.127274.

[31] Z. Rahmati, H. Jamshidi Aval, S. Nourouzi, R. Jamaati, Effect of mechtrode rotational speed on friction surfacing of AA2024 on AA1050 substrate, CIRP J. Manuf. Sci. Technol. 33 (2021) 209–221, http://dx.doi.org/10.1016/j.cirpj.2021.03.012.

[32] M. Hoffmann, A. Roos, B. Klusemann, Investigation of microstructural and mechanical properties in AA2024-T351 multi-layer friction surfacing, Surf. Coat. Technol. 480 (2024) 130610, http://dx.doi.org/10.1016/j.surfcoat.2024.130610.

[33] K.K. Jha, R. Kesharwani, M. Imam, Microstructure and mechanical properties correlation of FSAM employed AA5083/AA7075 joints, Trans. Indian Inst. Met. 76 (2023) 323–333, http://dx.doi.org/10.1007/s12666-022-02672-9.

[34] M.I. Latypov, M. Kühbach, I.J. Beyerlein, J.-C. Stinville, L.S. Toth, T.M. Pollock, S.R. Kalidindi, Application of chord length distributions and principal component analysis for quantification and representation of diverse polycrystalline microstructures, Mater. Charact. 145 (2018) 671–685, http://dx.doi.org/10.1016/j.matchar.2018.09.020.

[35] R. Armstrong, 60 Years of Hall-Petch: past to present nano-scale connections, Mater. Trans. 55 (1) (2014) 2–12, http://dx.doi.org/10.2320/matertrans.MA201302.

[36] J. Gandra, P. Vigarinho, D. Pereira, R.M. Miranda, A. Velhinho, P. Vilaça, Wear characterization of functionally graded Al–SiC composite coatings produced by friction surfacing, Mater. Des. (1980-2015) 52 (2013) 373–383, http://dx.doi.org/10.1016/j.matdes.2013.05.059.